Joint interpretation, joint inversion, and sequential inversion of different geophysical datasets: two case studies in Iran and South Africa

A.D. Mongabadi[1], A.Z. Shirvanehdeh[2], A. Nasseri[3] and R. Pourmirzaee[4]

[1] Department of Mining Engineering, Ahar Branch, Islamic Azad University, Ahar, Iran
[2] Department of Civil Engineering, Shabestar Branch, Islamic Azad University, Shabestar, Iran
[3] Department of Mining Engineering, Ahar Branch, Islamic Azad University, Ahar, Iran
[4] Department of Mining Engineering, Urmia University of Technology, Urmia, Iran

ABSTRACT This paper employs various combinations of geophysical data, including sequential inversion, joint interpretation, and joint inversion, to analyse two case studies in Iran and South Africa. The selection of integration types for geophysical datasets is dependent on the specific requirements of each case study. The first real case, which involves apparent resistivities and gravity gradient data to detect three tunnels, is particularly well suited for joint interpretation. The joint interpretation of reconstructed resistivity and density models serves as a reliable indicator of the accurate recovery of the tunnels. The second real case, comprising direct current (DC) resistivity, magnetometry, and electromagnetism at low induction number (EM-LIN) data, enables 1) the joint inversion of DC resistivity and magnetometry and 2) the sequential inversion of DC resistivity and EM-LIN data. The inversion of DC resistivity data reveals a two-layered medium, where the upper layer exhibits high conductivity and the lower layer exhibits high resistivity. In contrast, the inversions of magnetometry and EM-LIN data indicate the presence of a resistive and magnetised dolerite dyke, with depth ranges spanning from 3 to 15 m. The resistivity models generated through joint and sequential inversions provide conclusive evidence of a dyke situated within a two-layered medium.

Key words: DC resistivity, joint interpretation, joint inversion, potential fields, sequential inversion.

1. Introduction

The primary objective in geophysics is to reconstruct the most accurate and detailed subsurface images from measured data, thereby, presenting a consistent interpretation that accurately reflects the real subsurface structure. This goal can be achieved through the application of quantitative interpretation techniques. The most widely adopted approach for quantitative interpretation in geophysics is the data inversion process. The necessity of reconstructing high-resolution images of underground sourceas has led geophysicists to integrate geophysical datasets, as individual inversions constrained by widespread constraints (e.g. smoothness and depth weighting) and *a priori* information often prove insufficient. The combination of different geophysical datasets can be achieved through three primary techniques: 1) joint interpretation, which involves integrating multiple datasets and various

models to provide a unified interpretational view of the subsurface structure (Ogaya *et al.*, 2016; Hosseini *et al.*, 2021; Milano *et al.*, 2021; Parnow *et al.*, 2021; Ghari *et al.*, 2023; Ghiasi *et al.*, 2023), 2) sequential inversion, where datasets are sequentially inverted to improve the resolution and accuracy of the final subsurface models (Le *et al.*, 2016; Varfinezhad *et al.*, 2023), and 3) joint inversion, which can be further categorised into two sub-techniques: joint inversion based on petrophysical constraints (e.g. Ghose and Slob, 2006; Varfinezhad *et al.*, 2016) and structural based joint inversion techniques (e.g. Gallardo and Meju, 2004; Molodtsov *et al.*, 2013; Joulidehsar *et al.*, 2018). Adopting the geophysical data integration type is crucial and should be tailored to the specific case. This research aims to investigate such issue.

Initially, various types of geophysical data combinations are briefly explained.

1.1. Joint interpretation

In the case of joint interpretation, inverted models of the involved approaches are independently recovered, and the interpretation is, then, made based on the individual inversions obtained and other available information, such as geological data. Joint interpretation is a subjective process, implying that two geophysicists might arrive at different interpretations (of the final models of subsurface structures). This subjectivity can be a significant disadvantage of this geophysical data combination type (Gallardo and Meju, 2004). However, these discrepancies may be insignificant for many cases. Therefore, the joint interpretation technique can be a reliable strategy for interpreting subsurface anomalies, as demonstrated by various studies (e.g. Orlando, 2005; Al Farajat, 2009; Karavul *et al.*, 2010; Sultan *et al.*, 2010; Gambetta *et al.*, 2011; Orfanos and Apostolopoulos, 2011; Zhang *et al.*, 2018; Ebrahimi *et al.*, 2019; Hosseini *et al.*, 2021; Milano *et al.*, 2021; Parnow *et al.*, 2021; Ghari *et al.*, 2023).

1.2. Sequential inversion

The concept of sequential inversion was initially introduced, without a well-defined and quantitative criterion, to establish similarities between two geophysical models (Gallardo and Meju, 2004). In this approach, the individual inversion of one geophysical dataset is obtained and, then, used as the initial model for the inversion of the second dataset. In other words, characteristics of the sources in the first inverted section constrain the inversion section of the second geophysical dataset. This type of geophysical data integration has been commonly employed for the combination of different datasets (e.g. Singh *et al.*, 2019; Varfinezhad *et al.*, 2023). A key disadvantage of the sequential inversion approach is that the final model tends to be biased towards one of the models rather than towards the other (Gallardo, 2004).

1.3. Joint inversion through the cross-gradient approach

Joint inversion based on structural similarities utilising the cross-gradient function has become increasingly common over the past two decades (e.g. Gallardo and Meju, 2004; Fregoso and Gallardo, 2009; Molodtsov *et al.*, 2013; Bennington *et al.*, 2015; Joulidehsar *et al.*, 2018). The joint inversion approach of arrival times and apparent resistivities was initially introduced by Gallardo and Meju (2003). Generally, this approach involves the simultaneous inversion of two different geophysical datasets while enforcing structural similarities between the resulting models. Following the initial introduction, the cross-gradient function has been extensively utilised for the joint inversion of diverse geophysical methods. Examples include the integration

of magnetotellurics and seismic data (Gallardo and Meju, 2007), gravity and magnetometry (Fregoso and Gallardo, 2009), as well as frequency domain electromagnetic and seismic data (Hu *et al.*, 2009). The cross-gradient constraint operates on the underlying assumption that the geophysical methods involved are capable of sensing the same geological structures (Gallardo and Meju, 2004).

1.4. Research aims and innovative techniques

In this study, the integration of the mentioned geophysical datasets is applied to two real-world case studies to demonstrate their effectiveness. In the first case, direct current (DC) resistivity and gravity gradient data are jointly inverted to detect a tunnel based on the joint interpretation. The objective of the second case study is to identify a dolerite dyke embedded within a layered medium as an indicator of the presence of groundwater at the Morgenzon Farm site in South Africa. This case study involves DC resistivity, magnetometry and electromagnetism at low induction number (EM-LIN) datasets. The analysis includes: i) the joint inversion of DC resistivity and magnetometry data through cross-gradient constraint, and ii) the sequential inversion of EM-LIN and DC resistivity data. The rationale for the selection of the specific geophysical datasets will be explained herein. Specifically, the reasons for choosing DC resistivity and magnetic data for joint inversion, as well as the rationale for using EM-LIN and DC resistivity data for sequential inversion, will be discussed.

This research presents three novel and interesting aspects. I) The joint inversion of DC resistivity and magnetometry data, using the cross-gradient constraint, has been previously conducted only by Varfinezhad *et al.* (2020). However, they employed an approximate method (linear equations) for the DC resistivity inversion, as introduced by Perez-Flores *et al.* (2001). In contrast, the current study utilises the exact approach (nonlinear equations) for the DC resistivity inversion, which differentiates the proposed algorithm from the previous work. Furthermore, Varfinezhad *et al.* (2020) employed depth weighting and compactness constraints for the separate inversion of DC resistivity data, as well as for its joint inversion with magnetometry data. In contrast, the current study utilises a smoothness constraint for both the separate and joint inversion procedures. II) To the best of our knowledge, the sequential inversion of DC resistivity and EM-LIN data has not been previously reported within the literature. III) The effectiveness of different geophysical data combinations is demonstrated through their application to two real-world case studies.

1.5. Outline and organisation of the paper

In the methodology section, the forward modelling and inversion of DC resistivity are described first as, unlike the other geophysical methods involved in this study, the DC resistivity modelling problem is nonlinear. Subsequently, the forward problems of the other approaches (magnetometry, gravity gradient and EM-LIN) are presented. Following the presentation of the forward problems, the individual inversion approaches adopted for these techniques are introduced. Ultimately, the joint interpretation, sequential inversion, and cross-gradient based joint inversion algorithm are explained. The application of joint interpretation, joint inversion, and sequential inversion to real datasets are presented in sections 3, 4, and 5, respectively. The rationale behind these choices is clearly explained in the Discussion section.

2. Methodology

2.1. Forward and inverse modelling of DC resistivity

DC resistivity forward modelling is a nonlinear problem due to the nonlinearity of the Maxwell equations with respect to resistivity (Varfinezhad and Oskooi, 2020). As a result, the forward problem can be represented with the following equation:

$$\mathbf{F}(\mathbf{m}) = \mathbf{d}. \tag{1}$$

The model parameter vector, data vector, and nonlinear forward operator are denoted by $\mathbf{m}$, $\mathbf{d}$, and $\mathbf{F}$, correspondingly. The inversion of DC resistivity data can be accomplished by minimising an objective function, as specified in the following equation:

$$min \;\rightarrow\; \|W_d(F(m) - d)\|_2^2 + \mu\|W_m(m - m_0)\|_2^2. \tag{2}$$

Variables $\mathbf{d}$, $\mathbf{F(m)}$, $\mathbf{m_0}$, and $\mathbf{m}$ correspond to the observed data, calculated forward response, initial model estimate, and final inverted model, correspondingly. $\mathbf{W_d}$ and $\mathbf{W_m}$ symbolise the data and model weighting matrices, and μ indicates the regularisation parameter. Commonly, data weighting matrix $\mathbf{W_d}$ is constructed as a diagonal matrix, where data points with smaller associated errors are given higher weights during the inverse process. The model weighting matrix, $\mathbf{W_m}$, is chosen to be a smoothness matrix, and consequently, the inversion method utilised is a smoothness-constrained algorithm, as described below:

$$\mathbf{m} = \mathbf{m_0} + (\mathbf{J^T J} + \mu_k \mathbf{W_m})^{-1} \mathbf{J^T}[(\mathbf{d} - \mathbf{F(m)}]. \tag{3}$$

The Jacobian matrix, $\mathbf{J}$, is defined explicitly in Eq. (4). Assuming forward operator $\mathbf{F}$ and model parameter vector $\mathbf{m}$ each have M×N components, the Jacobian matrix will be of dimensions M×N and can be computed using the equation provided (Aster *et al.*, 2018):

$$\mathbf{J} = \begin{bmatrix} \dfrac{\partial \mathbf{F_1(m)}}{\partial \mathbf{m_1}} & \cdots & \dfrac{\partial \mathbf{F_1(m)}}{\partial \mathbf{m_N}} \\ \vdots & \ddots & \vdots \\ \dfrac{\partial \mathbf{F_M(m)}}{\partial \mathbf{m_1}} & \cdots & \dfrac{\partial \mathbf{F_M(m)}}{\partial \mathbf{m_N}} \end{bmatrix}. \tag{4}$$

The iterative inverse process begins with an initial homogenous model, $\mathbf{m_0}$, where the resistivity is set equal to the mean value of the observed apparent resistivities. Then, the Jacobian matrix is computed, and inverse model $\mathbf{m}$ is obtained through Eq. (3). This retrieved model is used as the initial model for the next iteration, and inverse model $\mathbf{m}$ is computed again. The iterative inverse process continues until the desired root-mean-square (RMS) misfit error, or the maximum number of iterations, is achieved.

2.2. Forward problem of magnetometry

To enable the numerical computation of magnetic modelling, the subsurface of the target region is partitioned into a multitude of prisms that are infinitely extended along a single

direction (in this instance, the *y*-axis). It is assumed that the magnetic susceptibility remains constant within each prism (analogous to Fig. 1). The forward response of a magnetic source can be evaluated by employing Eq. (5) (Blakely, 1996).

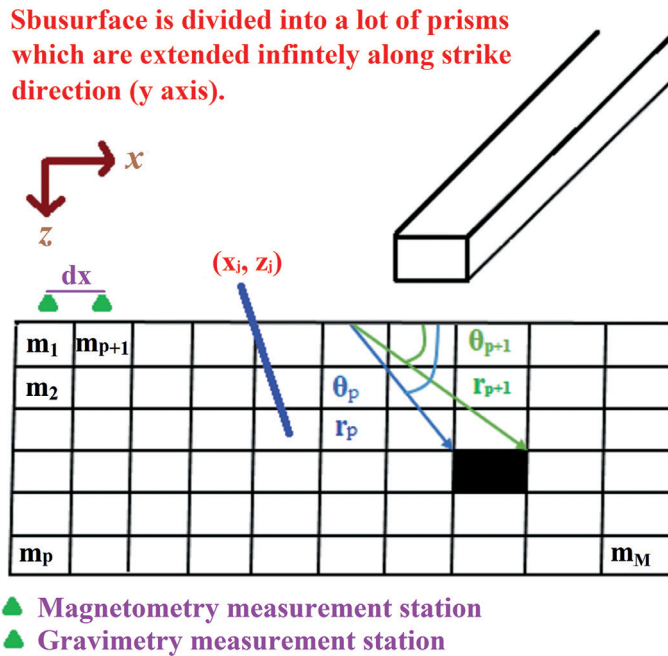$$d_i = \sum_{j=1}^{M} \sum_{k=1}^{4} (\hat{f}_x B_x^l + \hat{f}_z B_z^l)_i \ .$$

(5)

Sbusurface is divided into a lot of prisms which are extended infintely along strike direction (y axis).

Fig. 1 - Discretisation of subsurface into a multitude of prisms which are infinitely extended along the strike direction.

Variable d_i is used to express the predicted magnetic response at the *i*-th location within the study area. Unit vector components $\hat{f}_x$ and $\hat{f}_z$ are employed to account for the orientation of the geomagnetic field along the *x* and *z* axes. Variables B_x^l and B_z^l are used to represent the *x* and *z* components of the magnetic field, which are mathematically defined by Eqs. (6) and (7):

$$B_x = -2C_m (M.\hat{n})[\hat{s}_x \log\left(\frac{r_2}{r_1}\right) - \hat{s}_z(\theta_1 - \theta_2)]$$

(6)

$$B_z = -2C_m (M.\hat{n})[\hat{s}_z \log\left(\frac{r_2}{r_1}\right) + \hat{s}_x(\theta_1 - \theta_2)]$$

(7)

r_1, r_2, θ_1 and θ_2 are depicted in Fig. 1, $\hat{n}$ refers to unit vector which is vertical to each prism, $\hat{s}_x = \widehat{n_z}$, $\hat{s}_z = \widehat{n_x}$, and $C_m = \frac{\mu_0}{4\pi} = 10^{-7}$ in SI units.

Numerical calculation of Eq. (5) can be expressed in the form of matrix Eq. (8):

$$\mathbf{d}_M = \mathbf{A}_M \mathbf{m}_M$$

(8)

where $\mathbf{A_M}$ is the forward operator matrix and $\mathbf{m_M}$ and $\mathbf{d_M}$ express the vectors of the model parameters and the observed magnetic anomaly, respectively.

2.3. Forward problem for gravity gradient data

The two-dimensional (2D) forward problem of gravimetry can be obtained through Eq. (9). In this regard, the subsurface can again be discretised into numerous prisms that extend infinitely along the strike direction (i.e. the *y*-axis), and the density contrast can be assumed to be constant within each prism (as shown in Fig. 1). Under these assumptions, the forward response of a gravity anomaly can be computed using the formulation provided by Last and Kubic (1983):

$$d_i = \sum_{j=1}^{M} A_{ij} m_j \qquad i = 1.2. \dots . N \tag{9}$$

d_i is the *i*-th calculated data, A_{ij} is an element of the kernel matrix (forward operator) representing the *j*-th cell effect on the *i*-th data, m_j is the density contrast of the *j*-th cell.

A_{ij} values can also be calculated utilising Eq. (10) (Last and Kubic, 1983):

$$A_{ij} = 2G\left[\left(x_i - x_j + \frac{dx}{2}\right) log\left(R_2 R_3 / R_1 R_4\right) + dx \, log\left(R_4 / R_3\right) - \left(z_j + \frac{dz}{2}\right)\right.$$
$$\left. (T_4 - T_2) + \left(z_j - \frac{dz}{2}\right)(T_3 - T_1)\right] \tag{10}$$

where *dx* and *dz* are side lengths of prisms along the *x* and *z* axes, and x_i is the location of measurements along the profile. *G* denotes the gravitational constant, and *R* and *T* can be computed using the following equations (Last and Kubic, 1983):

$$R_1^2 = (z_j - \tfrac{dz}{2})^2 + (x_i - x_j + \tfrac{dx}{2})^2 \qquad\qquad T_1 = \arctan\,(x_i - x_j + \tfrac{dx}{2})/(z_j - \tfrac{dz}{2})$$

$$R_2^2 = (z_j + \tfrac{dz}{2})^2 + (x_i - x_j + \tfrac{dx}{2})^2 \qquad\qquad T_2 = \arctan\,(x_i - x_j + \tfrac{dx}{2})/(z_j + \tfrac{dz}{2})$$

$$R_3^2 = (z_j - \tfrac{dz}{2})^2 + (x_i - x_j - \tfrac{dx}{2})^2 \qquad\qquad T_3 = \arctan\,(x_i - x_j - \tfrac{dx}{2})/(z_j - \tfrac{dz}{2})$$

$$R_4^2 = (z_j + \tfrac{dz}{2})^2 + (x_i - x_j - \tfrac{dx}{2})^2 \qquad\qquad T_4 = \arctan\,(x_i - x_j - \tfrac{dx}{2})/(z_j + \tfrac{dz}{2})\ .$$

Similarly, the forward problem can be expressed as:

$$\mathbf{d = Am} \tag{11}$$

where $\mathbf{A}$ represents the forward operator of gravimetry, $\mathbf{m}$ denotes the model vector (containing density values in the prisms), and $\mathbf{d}$ indicates the data vector (observed gravity anomaly). To calculate the forward response at a specific height, *h*, it suffices to transform the depth of each prism, z_j, to $z_j + h$.

The variation of gravity components along the three spatial directions produces the gravity gradient tensor. The most commonly used component is the vertical gravity gradient, g_{zz}, which

represents the rate of change of the vertical gravity component at height z. The value of the vertical gravity gradient, g_{zz}, can be deduced from the difference between the gravity values at two points separated by a small vertical distance, h:

$$g_{zz} = \frac{\partial \mathbf{d}}{\partial z} \approx \frac{\mathbf{d}(z+h/2)-\mathbf{d}(z-h/2)}{h}.$$
(12)

Gravity modelling takes the form of a Fredholm integral equation (IE) of the first kind, making it a linear problem. The modelling of the vertical gravity gradient, g_{zz}, is also a linear problem, and its matrix form can be expressed using the following equation:

$$\mathbf{d}_G = \mathbf{A}_G \mathbf{m}_G$$
(13)

where $\mathbf{d}_G$ represents the data vector of observed vertical gravity gradient (g_{zz}) values. $\mathbf{A}_G$ is the forward operator, and $\mathbf{m}_G$ is the density model.

2.4. Forward problem of EM-LIN

Perez-Flores *et al.* (2001) pioneered an IE based approach for EM-LIN modelling, which includes both horizontal and vertical magnetic dipoles. These IEs can be classified as Fredholm IEs of the first kind, where apparent conductivities σ_a (observed data) exhibit a linear relationship with true conductivities $\sigma(r)$ (model parameters). Since this research focuses on the use of horizontal magnetic dipoles (HMD), only the equations, required for the HMD configuration, are presented:

$$\sigma_a(r_1, r_2) = -\frac{16\pi s}{\omega \mu_0 m_y} \iint_v G_{Hy}(r, r_2) . E_{Hy}(r, r_1) \sigma(r) d^3 r$$
(14)

where s represents the transmitter-receiver (T-R) separation, ω denotes the angular frequency, μ_c is the magnetic permeability, and m_y is the magnetic moment around the y-direction. Position vectors r_1, r_2, and r correspond to the locations of the transmitter, receiver, and subsurface, respectively (as shown in Fig. 2). The appropriate equations for $G_{Hy}(r, r_2)$ and $E_{Hy}(r, r_1)$ can be found in Table 1.

Table 1 - Required functions for HMD configuration (Perez-Flores *et al.*, 2001).

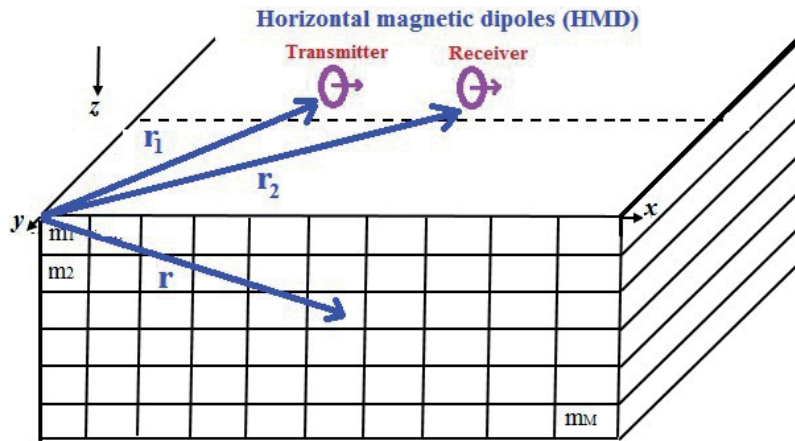| Function	Formula
G_{H_y}	$\frac{1}{4\pi}\left\{\left[\frac{1}{\rho_2^2}-\frac{z+h}{\rho_2^2\|r-r_2\|}-\frac{2(y-y_2)^2}{\rho_2^4}+\frac{2(z+h)(y-y_2)^2}{\rho_2^4\|r-r_2\|}+\frac{(z+h)(y-y_2)^2}{\rho_2^2\|r-r_2\|^3}\right]i+\left[\frac{(x-x_2)(y-y_2)}{\rho_2^2}\left(\frac{2}{\rho_2^2}-\frac{2(z+h)}{\rho_2^2\|r-r_2\|}-\frac{z+h}{\|r-r_2\|^3}\right)\right]j\right\}$
E_{H_y}	$\frac{\omega\mu_0 m_y}{4\pi}\left\{\left[\frac{1}{\rho_1^2}-\frac{z+h}{\rho_1^2\|r-r_1\|}-\frac{2(y-y_1)^2}{\rho_1^4}+\frac{2(z+h)(y-y_1)^2}{\rho_1^4\|r-r_1\|}+\frac{(z+h)(y-y_1)^2}{\rho_1^2\|r-r_1\|^3}\right]i+\left[\frac{(x-x_1)(y-y_1)}{\rho_1^2}\left(\frac{2}{\rho_1^2}-\frac{2(z+h)}{\rho_1^2\|r-r_1\|}-\frac{z+h}{\|r-r_1\|^3}\right)\right]j\right\}$

Fig. 2 - Illustration of the subsurface area, which is divided into numerous prisms of infinite length along the *y*-axis.

Eq. (14) requires discretisation to enable numerical modelling. Therefore, the subsurface area is divided into numerous prisms that infinitely extend along the strike direction (e.g. *y*-axis), and the mid-point rule can be used to discretise Eq. (14) (Varfinezhad *et al.*, 2022). As a result, the previous equation can be reduced to a matrix equation as follows:

$$\mathbf{d}_E = \mathbf{A}_E \mathbf{m}_E \tag{15}$$

where $\mathbf{d}_E$ and $\mathbf{m}_E$ define the data and model vectors, respectively, and $\mathbf{A}_E$ represents the forward operator. For more details about the 2D forward modelling of the EM-LIN method, readers are referred to the paper by Perez-Flores *et al.* (2001).

2.5. Inversion of magnetometry, gravity gradient and EM-LIN

Magnetic, gravity gradient, and EM-LIN modelling problems are linear in nature. Therefore, a general inversion algorithm is used for all of them, with some differences that will be clearly explained. The non-uniqueness and instability of geophysical inverse problems require regularisation in terms of *a priori* information and constraints, such as smoothness, compactness, and depth weighting, which are incorporated into the inverse procedure. Tikhonov and Arsenin (1977) introduced a general formula as an objective function which demands to be minimised:

$$\min \; \rightarrow \; \|\mathbf{W_d}(\mathbf{Gm} - \mathbf{d})\|_2^2 + \alpha \|\mathbf{W_m}(\mathbf{m} - \mathbf{m_0})\|_2^2 \; . \tag{16}$$

The first term in the objective function expresses the weighted data misfit, where $\mathbf{W_d}$ is the covariance matrix. The second term is used for the regularisation, which is weighted by the model weighting matrix $\mathbf{W_m}$. The term $\mathbf{m_0}$ defines the initial model, which is constructed using *a priori* information such as a geological model, the inverse model of other geophysical methods, and so on.

The contribution of the regularisation term in the inverse model is determined by regularisation parameter α. A large value of α leads to a more stable inverse model, but the resolution of the obtained inverse model decreases.

Conversely, a small value of α produces a model with lower stability but higher resolution.

Therefore, the estimation of the regularisation parameter (α) requires a trade-off between stability and resolution (Aster *et al.*, 2018). The L-curve and generalised cross-validation are two widely used techniques to estimate the regularisation parameter.

Over the past decades, various algorithms have been proposed for the single inversion of magnetometry, gravity gradient, and EM-LIN data (e.g. Li and Oldenburg, 1996; Boulanger and Chouteau, 2001; Perez-Flores *et al.*, 2001, 2012; Cella and Fedi, 2012; Paoletti *et al.*, 2013; Parnow *et al.*, 2021). However, in this paper, the damped weighted minimum length solution algorithm, introduced by Varfinezhad *et al.* (2020), was utilised:

$$\mathbf{m} = \mathbf{m}_0 + (\mathbf{W_m^{-1}G^T})(\mathbf{GW_m^{-1}G^T} + \alpha\mathbf{W_d})^{-1}(\mathbf{d} - \mathbf{Gm}_0) \, . \tag{17}$$

For the magnetometry and gravity gradient approaches, the reference model, $\mathbf{m}_0$, is assumed to be zero during the iterative inversion process (Last and Kubik, 1983; Milano *et al.*, 2021). In contrast, for the EM-LIN method, the initial model, $\mathbf{m}_0$, is a homogeneous model with a conductivity value equal to the mean of the observed apparent conductivities (Parnow *et al.*, 2021).

The model weighting matrix, $\mathbf{W}_m$, plays a crucial role in obtaining the inverse model, which is defined as follows.

For the EM-LIN approach, model weighting matrix $\mathbf{W}_m$ is defined as a depth weighting function, specifically, $\mathbf{W}_m = \frac{1}{Z^\beta}$, where Z represents the vector of z-coordinates of the prism centres and β is the exponent that defines depth weighting (Varfinezhad and Parnow, 2021).

For the magnetometry and gravity gradient methods, model weighting matrix $\mathbf{W}_m$ is defined as the product of two components: depth weighting ($\frac{1}{Z^\beta}$) and compactness constraints ($\frac{1}{(m+eps)^2}$), where Z represents the vector of depth coordinates, β is the depth weighting exponent, and $\mathbf{m}$ is the inverse model (Last and Kubik, 1983; Li and Oldenburg, 1996).

The depth weighting exponent is assumed to be equal to unity for all approaches, as it is considered the optimal choice for 2D cases.

The flowchart depicted in Fig. 3 illustrates the manipulation of the inverse algorithm for the inversion of these methods.
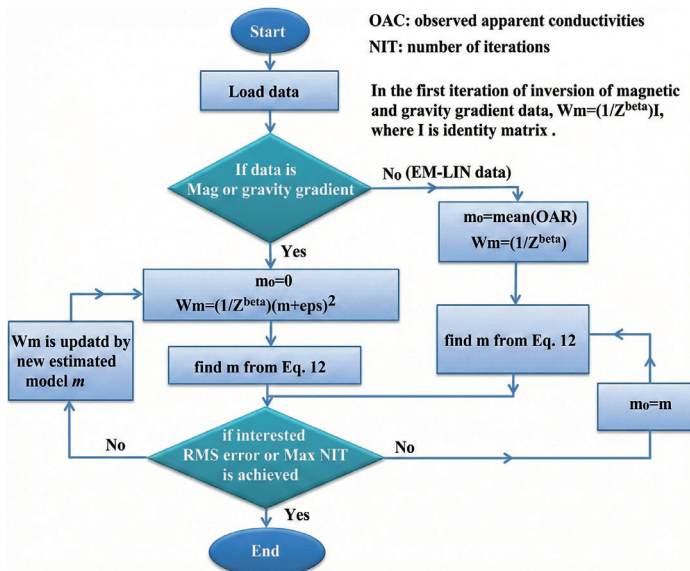

Fig. 3 - Flowchart of the inverse algorithm for magnetic, gravity gradient and EM-LIN datasets. OAR = observed apparent resistivities.

2.6. Joint interpretation and sequential inversion

The joint interpretation and sequential inversion procedures are illustrated in Figs. 4 and 5, respectively. For the joint interpretation approach, separate inversions of the datasets involved are obtained, and the ultimate model of the subsurface is presented based on these inverse models, as well as on geological and other *a priori* information.

In the sequential inversion approach, the inversion model obtained from the first dataset is used as the initial model for the inversion of the second dataset. In this case, the inversion of the first dataset, along with any available geological constraints, are utilised as the starting point for the inversion of the second dataset.
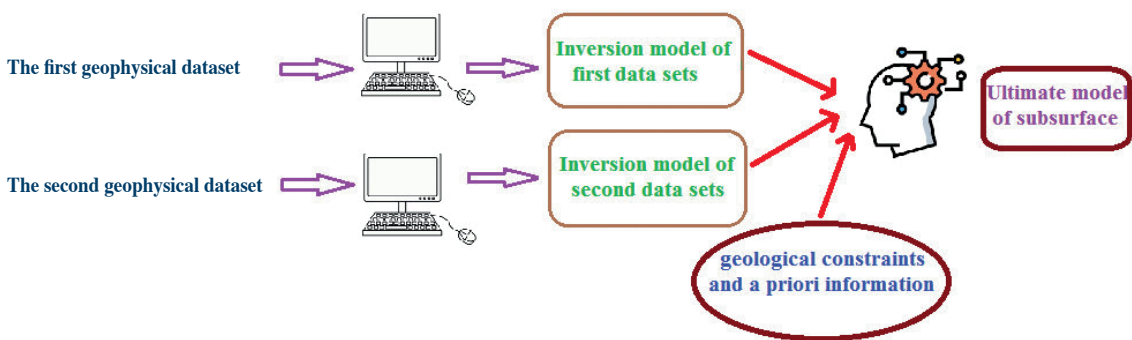

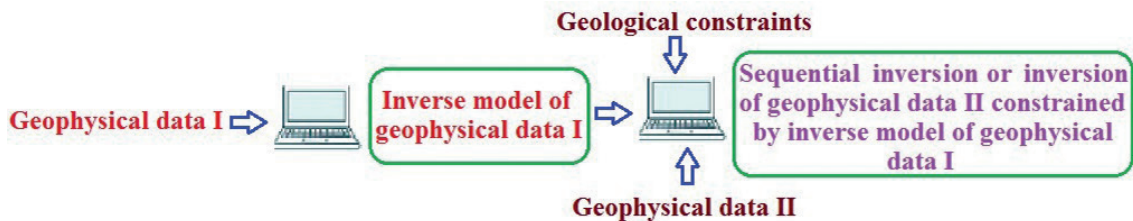Fig. 4 - Joint interpretation process of two arbitrary geophysical datasets.

Fig. 5 - Sequential inversion of two arbitrary geophysical datasets.

2.7. Cross-gradient joint inversion

Gallardo and Meju (2004) established the framework for joint inversion through the cross-gradient function, applicable to two arbitrary geophysical approaches. Since the goal is to implement the joint inversion of DC resistivity and magnetic data, the associated formulae for this joint inversion approach are presented.

For the 2D case, the cross-gradient function for the joint inversion of DC resistivity and magnetometry can be defined according to Eq. (18):

$$\boldsymbol{\tau} = \nabla \mathbf{m}_R(x, z) \times \nabla \mathbf{m}_M(x, z) \tag{18}$$

where $\mathbf{m}_M$ (x, z) and $\mathbf{m}_R$ (x, z) denote the susceptibility and resistivity models, respectively. The cross-gradient function τ is clearly expressed as described by Gallardo and Meju (2004):

$$\tau(x,z) = \left(\frac{\partial \mathbf{m}_R(x,z)}{\partial z}\right)\left(\frac{\partial \mathbf{m}_M(x,z)}{\partial x}\right) - \left(\frac{\partial \mathbf{m}_R(x,z)}{\partial x}\right)\left(\frac{\partial \mathbf{m}_M(x,z)}{\partial z}\right). \tag{19}$$

Larger values of the cross-gradient function indicate lower structural similarity between the involved inverse models, and vice versa. From the condition τ (x, z) = 0, two conclusions can be drawn: 1) at least one method senses no anomaly (i.e. $\nabla \mathbf{m}_R$ = 0 or $\nabla \mathbf{m}_M$ = 0, or both), and 2) the two models are completely similar, meaning any spatial variations should occur in the same way for both models (Varfinezhad *et al.*, 2020). Discretising Eq. (19), using a finite difference approach, produces Eq. (20), as described by Gallardo and Meju (2004):

$$\tau \cong \frac{4}{\Delta x \Delta z}\left(\mathbf{m}_{Rc}(\mathbf{m}_{Mb} - \mathbf{m}_{Mr}) + \mathbf{m}_{Rr}(\mathbf{m}_{Mc} - \mathbf{m}_{Mb}) + \mathbf{m}_{Rb}(\mathbf{m}_{Mr} - \mathbf{m}_{Mc})\right). \tag{20}$$
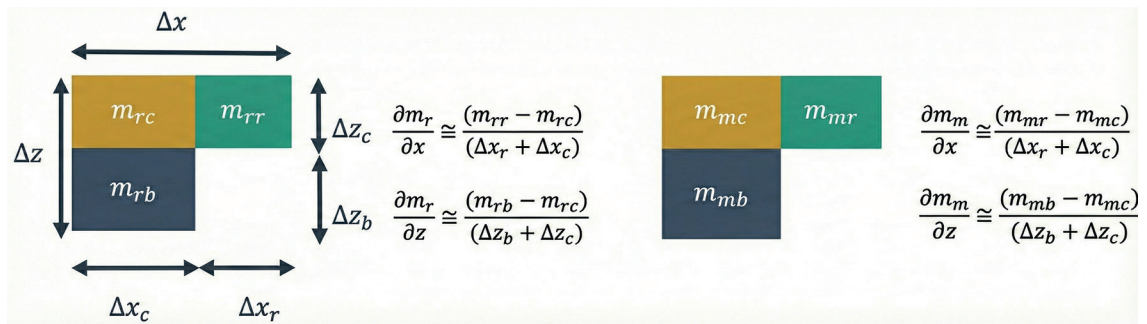

Fig. 6 -The three-cell layout to determine the discrete version of the cross-gradients.

For any specified cell (designated with subscript c), the bottom and right closest cells are defined by subscripts b and r, respectively (as shown in Fig. 6). The nonlinear 2D cross-gradient-based joint inversion problem of DC resistivity and magnetometry is solved using an algorithm that is nearly identical to the one introduced by Gallardo and Meju (2004):

$$\mathbf{m} = \mathbf{N}_1^{-1}\mathbf{n}_2 - \mathbf{N}_1^{-1}\mathbf{B}^{\mathrm{T}}(\mathbf{B}\mathbf{N}_1^{-1}\mathbf{B}^{\mathrm{T}})^{-1}(\mathbf{B}\mathbf{N}_1^{-1}\mathbf{n}_2 - \mathbf{B}\mathbf{m}_0 + \mathbf{t}_0) \tag{21}$$

where

$$\mathbf{N}_1 = \begin{bmatrix} \mathbf{J}_R^{\mathrm{T}}\mathbf{W}_{eR}\mathbf{J}_R + \alpha_R^2\mathbf{W}_{mR} & 0 \\ 0 & \mathbf{A}_M^{\mathrm{T}}\mathbf{W}_{eM}\mathbf{A}_M + \alpha_M^2\mathbf{W}_{mM} \end{bmatrix} \tag{22}$$

and

$$\mathbf{n}_2 = \begin{bmatrix} \mathbf{J}_R^{\mathrm{T}}\mathbf{W}_{eR}\{\mathbf{d}_R - F(\mathbf{m}_{0R})\} \\ \mathbf{A}_M^{\mathrm{T}}\mathbf{W}_{eM}\{\mathbf{d}_M - \mathbf{A}_M\mathbf{m}_{0M}\} \end{bmatrix}. \tag{23}$$

The apparent resistivity data are denoted by $\mathbf{d}_R$, while the measured magnetic data are represented by $\mathbf{d}_M$. The data covariance matrices are $\mathbf{W}_{eR}$ and $\mathbf{W}_{eM}$, respectively. The smoothness constraint is denoted by $\mathbf{W}_{mR}$, and $\mathbf{W}_{mM}$ is obtained by multiplying the depth weighting (Li and Oldenburg, 1996) by the compacting (Last and Kubik, 1983) terms. The Jacobian matrices for the resistivity and magnetic forward operators are $\mathbf{J}_R$ and $\mathbf{A}_M$, respectively. The resistivity and magnetic models are referred to as $\mathbf{m}_R$ and $\mathbf{m}_M$, respectively. The regularisation coefficients associated with the regularisation terms describing the resistivity and magnetometry methods, are α_R and α_M, respectively.

Matrix **B** corresponds to the Jacobian matrix associated with the cross-gradient function $\boldsymbol{\tau}$. The cross-gradient function $\boldsymbol{\tau}_0$ represents the initial model for resistivity and susceptibility ($\mathbf{m}_{0R}$ and $\mathbf{m}_{0M}$). The first term on the right-hand side of Eq. (21) corresponds to the separate inversion of both methods, while the second term expresses the cross-gradient-based joint inversion. The joint procedure begins with the separate inversion of magnetometry and DC resistivity data, and the initial models are updated in subsequent iterations. Next, **B** and $\boldsymbol{\tau}$ are computed from the separate inversions, and the joint models are ultimately estimated. The stability and convergence of the algorithm are controlled by regularisation coefficients α_R and α_M, which are determined through trial and error to ensure that the interested RMS misfit errors are satisfied.

3. Joint interpretation: DC resistivity and gravity gradient

To demonstrate the effectiveness of joint interpretation, a real-world case, involving DC resistivity and gravity gradient data, is considered. The DC resistivity data (using a dipole-dipole configuration) and vertical gravity gradient (g_{zz}) datasets were collected along the same profile in a region near Tehran city in Iran. The subsurface targets are three tunnels elongated in one horizontal direction. The spatial coordinates of the tunnels are given in Table 2.

Table 2 - Spatial coordinates of the three tunnels.

Right	Middle	Left	
54-57	43-47	23-26	X(m)
4-8	6-9	3-6	Z(m)

A simplified three-dimensional (3D) view of the study area, including the tunnels and profile location, is depicted in Fig. 7. The apparent resistivity data were collected with a spacing of 4 m and a range of n from 1 to 10. The vertical gravity gradient (g_{zz}) data were measured with a sample interval of 2 m along the profile, with a length of 72 m. To obtain the inverse models of both methods, the subsurface was discretised into 18×9 prisms with side lengths of 4 and 2 m, respectively, along the x and z axes. The measured DC resistivity and vertical gravity gradient (g_{zz}) datasets are shown in Fig. 8.

The individual inversion models obtained from both datasets can be observed in Fig. 9. The resistivity inverse section demonstrates three sources with very high resistivity values, yet it contains a number of errors in the recovery of the subsurface targets. Moreover, the resolutions of the reconstructed tunnels are relatively low. In more detail, the resistivity inverse model shows the rightmost tunnel in its correct position, while the other two tunnels are not clearly
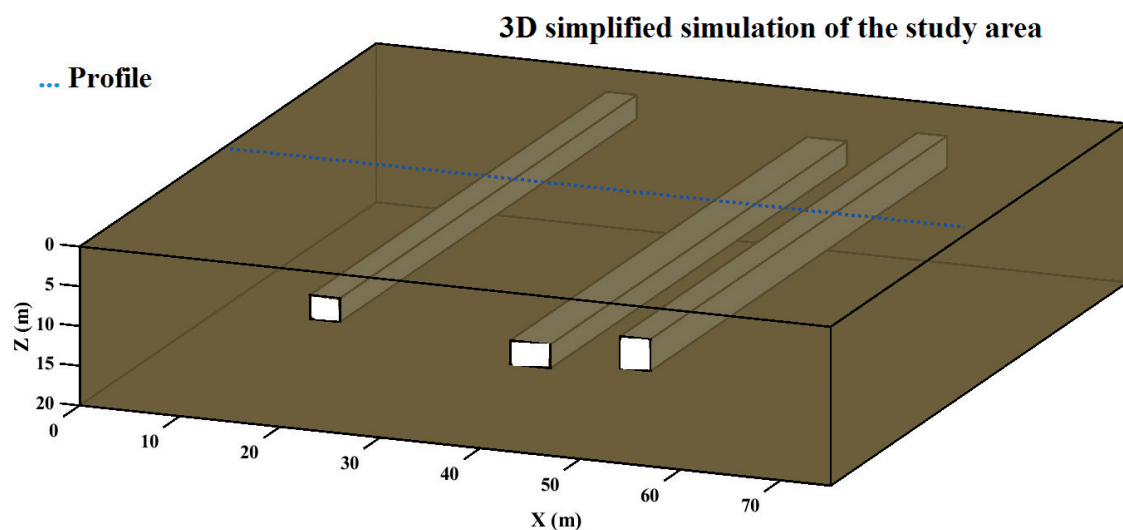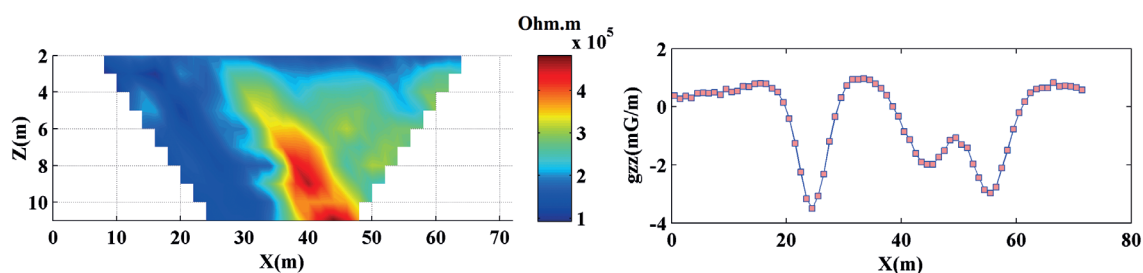
Fig. 7 - 3D view of the area including tunnels and profile location.

Fig. 8 - Pseudo section of the measured apparent resistivities (left) and vertical gravity gradient (g_{zz}) data (right).

distinguished from each other. Additionally, the depth range of the deepest tunnel shows some discrepancies with its true depth range.

In contrast, the inversion of the gravity gradient data shows a model where all sources are reconstructed with high resolution and approximately in their true positions. Considering both inverse models for joint interpretation provides sufficient confidence that three cavities or tunnels exist in the subsurface due to the very high resistivity values and negative density contrasts. Furthermore, the retrieved resistivity and density models exhibit good agreement regarding the horizontal and vertical extensions of the tunnels, although the resistivity section has
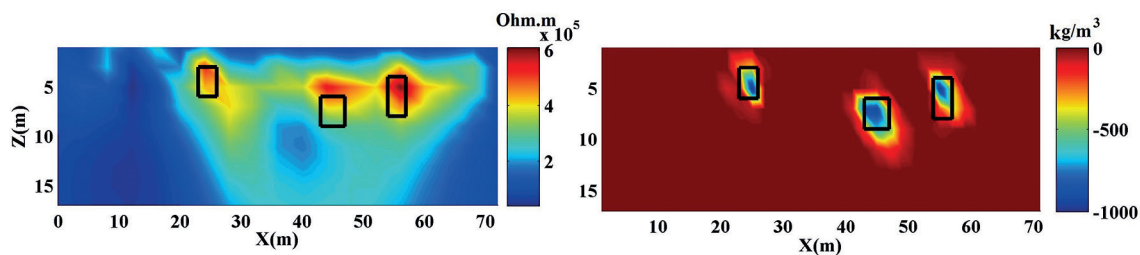

Fig. 9 - Inversion models for DC resistivity and gravity gradient data.

a significantly lower resolution compared to the density model. RMS misfit errors of computed data for DC resistivity and gravity gradient approaches are respectively 5.34% and 4.67%.

4. Joint inversion: DC resistivity and magnetometry

For the joint inversion process, the DC resistivity and magnetic datasets were collected along a profile in the Morgenzon Farm, which is one of the main sites of the Karoo Supergroup area in South Africa (Fig. 10). In the Karoo region, the key anomalies indicating the presence of groundwater are typically associated with dolerite dyke and sill structures (Vegter, 1992; Woodford and Chevallier, 2002).

4.1. Geology of the study area

The most common stratigraphy in South Africa is the Karoo Supergroup (McCarthy and Rubidge, 2005), which is formed of a thick sequence of predominantly sedimentary layers deposited between 310 and 182 million years ago (McCarthy and Rubidge, 2005). The sediments of the Karoo Supergroup are stratigraphically classified into several groups: the Dwyka, shaped by glacial deposition; the Ecca, formed by marine deposits; the Beaufort, created by fluvial deposition; and the Stormberg, formed by wind deposition (McCarthy and Rubidge, 2005). However, among these groups, the Drakensberg Group is the youngest stratigraphic unit, formed by the outflow of basaltic lavas (Makhokha and Fourie, 2016).
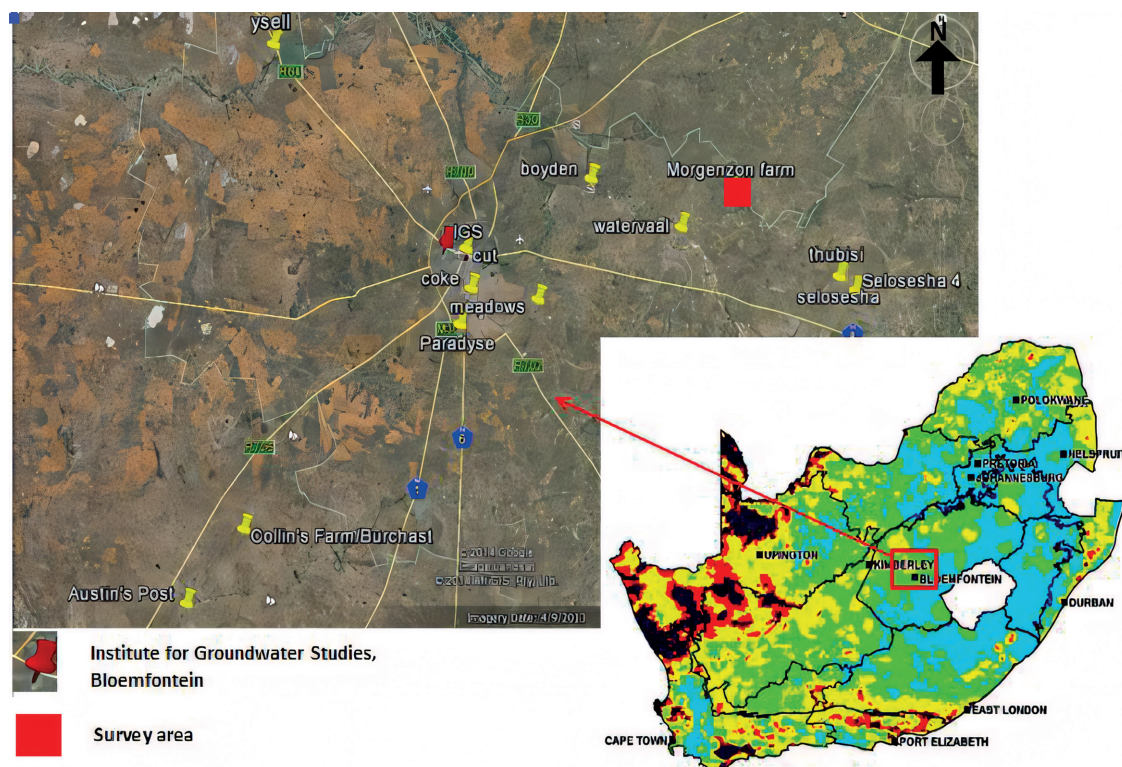

Fig. 10 - Satellite location of the study area (Makhokha and Fourie, 2016).

Compared to the relatively elastic siltstone and mudstone layers, the more inelastic sandstones in the Karoo formations are more susceptible to fracturing (Makhokha and Fourie, 2016). The predominant volcanism throughout the Jurassic period led to the primary fracturing of the Karoo rocks. Additionally, disregarding the Drakensberg lavas, the intrusion of dolerite laccoliths, sills, and dykes significantly contributed to the fracturing of the sedimentary rocks in the region (Makhokha and Fourie, 2016).

The large magnetic and resistive contrasts between dolerite structures and the surrounding sedimentary background make it feasible to employ simultaneous magnetometry and resistivity-based approaches (e.g. DC resistivity and electromagnetic induction) to effectively detect these structures.

4.2. Separate and joint inversion results

The profile of interest has a length of 400 m. A Wenner-Schlumberger array with electrode spacings of 5 and 10 m was employed to measure apparent resistivities. The data collection yielded 800 points, which were subsequently manipulated for individual and joint inversions. The magnetic data consisted of 250 points, although their sampling intervals were not identical (all were less than 2 m). The simultaneous individual and joint inversions of DC resistivity and magnetic data began with a homogeneous initial model, where the resistivity was set equal to the mean value of the measured apparent resistivities, and a reference model for magnetometry with zero susceptibility. Fig. 11 illustrates the individual and joint inversion models for both DC resistivity and magnetometry. The individual inversion of the DC resistivity data yields a two-layered model (interface model), whereas the magnetometry inversion reconstructs a dyke anomaly extending from near the surface to depths close to 15 m. The cross-gradient constraint serves as a robust tool in the joint inversion process, enabling the magnetometry data to contribute its useful information to the resistivity section. As a result, the dyke model is explicitly reconstructed in the resistivity model following the joint inversion procedure. Notably, the DC
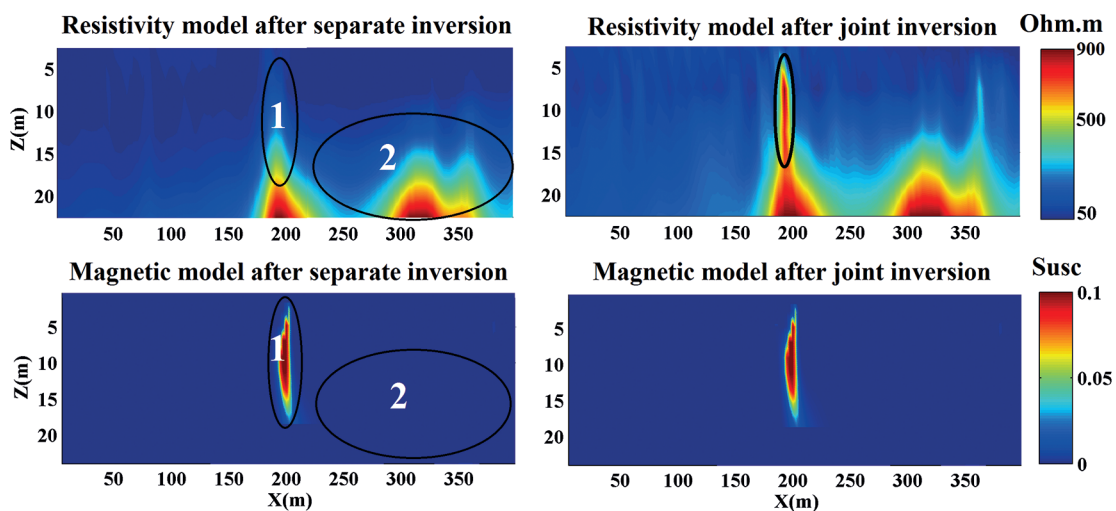

Fig. 11 - Separate and join inverse models for both DC resistivity and magnetometry approaches. Region 1: gradient of both models are non zeros, therefore, cross-gradient is useful, Region 2: gradient of magnetic is zero, therefore, cross-gradient cannot be helpful.
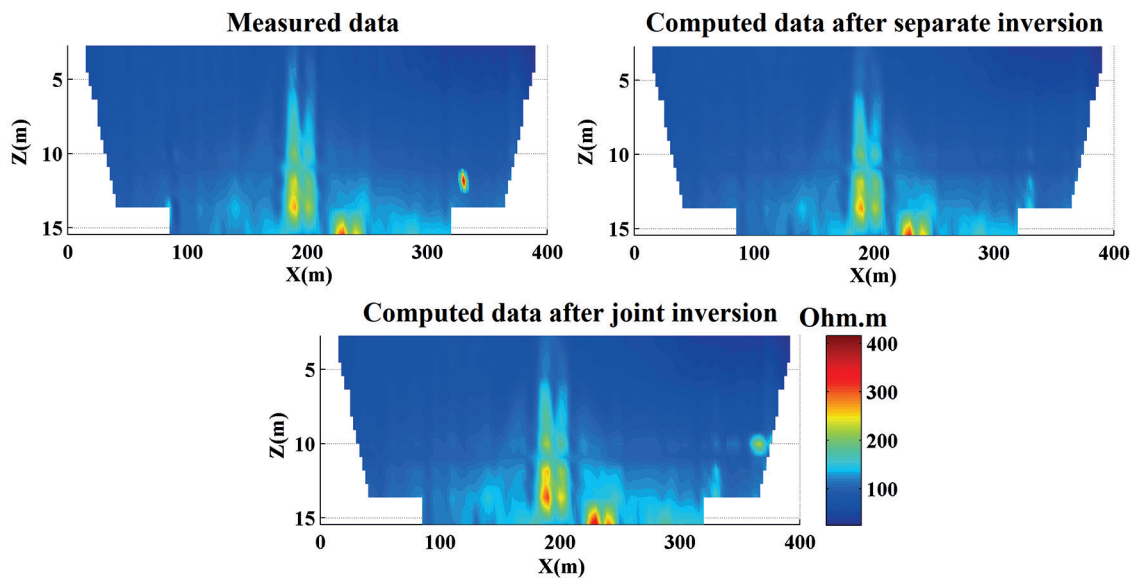
Fig. 12 - Pseudo sections of the measured apparent resistivities and computed apparent resistivities after separate and joint inversion procedures.

resistivity data is unable to assist the magnetometry inversion in recovering the interface model through the cross-gradient constraint.

4.3. Mathematical justification of joint results

Why does magnetometry help to improve DC resistivity after the joint process, but DC resistivity cannot help to improve the magnetic inverse section after the joint inversion? In this study, we want to address these observations from a mathematical point of view.

In the dyke position (middle of the profile), gradient of resistivities (individual inversion section) are not zero (i.e. $\nabla \mathbf{m}_R (x, z) \neq \mathbf{0}$) and the same is true for the individual inverse section of magnetometry (i.e. $\nabla \mathbf{m}_M (x, z) \neq \mathbf{0}$). For this reason, the cross-gradient function is useful and enables the magnetic method to improve the resistivity section after joint inversion. Conversely, the cross gradient could not transfer the layered model from the resistivity model to the susceptibility section after the joint inversion process, as the gradient of the susceptibility model in the right part is zero ($\nabla \mathbf{m}_M (x, z) = \mathbf{0}$) and $\boldsymbol{\tau} = \nabla \mathbf{m}_R \times \nabla \mathbf{m}_M = \mathbf{0}$. So, cross-gradient constraint cannot be useful for this case. Indeed, when one of the involving approaches does not sense an anomaly, other methods cannot be helpful in improving it through cross-gradient based joint inversion. All these numerical results are completely consistent with the mathematical properties of joint inversion through cross-gradient constraint.

Fig. 12 displays measured apparent resistivities and computed apparent resistivities after separate and joint inversions. RMS errors of data computed from separate and joint inverse models are 2.3% and 3.1%, respectively, which may be reasonable as for the joint model an additional constraint (cross-gradient function) is also manipulated. Extra constraint may result in more bias and, consequently, larger misfit may be obtained. Fig. 13 shows computed data after individual and joint inversions compared to measured data for the magnetometry method, demonstrating the same results with a RMS error of 5.46%, due to the identical inversion models after both individual and joint inversions.
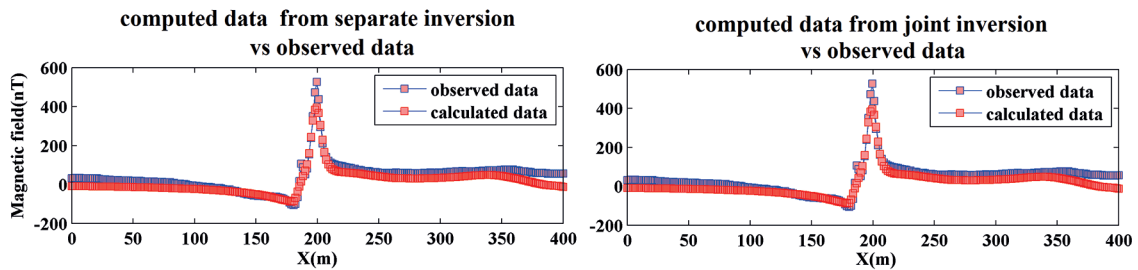
Fig. 13 - Computed data after individual and joint inversions compared to measured data.

5. Sequential inversion: DC resistivity and EM-LIN

We combine the DC resistivity and EM-LIN datasets from the Morgenzon Farm through a sequential inversion process. The EM-LIN data were collected using a horizontal magnetic dipole (HMD) configuration with a 10-metre sample interval and a 20-metre T-R separation along a 400-metre profile. For the DC resistivity data, which is common to both joint and sequential inversions, two key points should be clarified: 1) for the individual inversion of DC resistivity and its sequential inversion with EM-LIN data, 900 apparent resistivities (against the 800 used in the previous case) are used, and 2) both apparent resistivities and inverse models are displayed on a log10 scale.

We anticipate seeing some variations between the resistivity models presented here and the previous case. Why were these modifications made? They were made to demonstrate that more data points with a larger dipole separation of 20 m may be beneficial for constraining greater depths in the resistivity section, however, they may not be useful for reconstructing the dolerite dyke near the surface. Furthermore, the differences between resistivity sections in normal and logarithmic scales are negligible, indicating that the reliability of our inverse code is independent of the representation scale.

The measured datasets for both the EM-LIN and DC resistivity approaches are shown in Fig. 14. Fig. 15 displays the individual inversions of EM-LIN and DC resistivity datasets, as well as the sequential inversion of the DC resistivity and EM-LIN approaches. The individual inverse modelling of the EM-LIN data reconstructs a thick, horizontally stretched resistive dyke (i.e. low conductivity) that extends from approximately 180 to 200 m in the horizontal direction and ranges in depth from near the surface to about 15 m. The single inversion of the measured apparent resistivities recovers an interface model with a fluctuating boundary that extends to depths less than 10 m in the middle of the profile. The sequential inverse section of the DC resistivity demonstrates both interface and dyke zones with good resolution.

Actually, this model shows sufficient improvement with respect to the individual inversion results (as an advantage of the sequential inversion). The thickness of the conductive layer on the left side of the area [first layer of the individual inverse model of DC resistivity (Fig. 15B)] decreases after sequential inversion (compare Figs. 15B and 15C), which is a result of the sequential inversion process. In essence, the EM-LIN inverse model introduces biases into the resistivity section, which is the primary drawback of sequential inversion.

The comparison between the resistivity models derived from the joint and sequential inversions shows extremely good agreement. In fact, the joint interpretation of these models explicitly expresses the presence of a resistive/magnetised dolerite dyke from 5 to 15 m deep
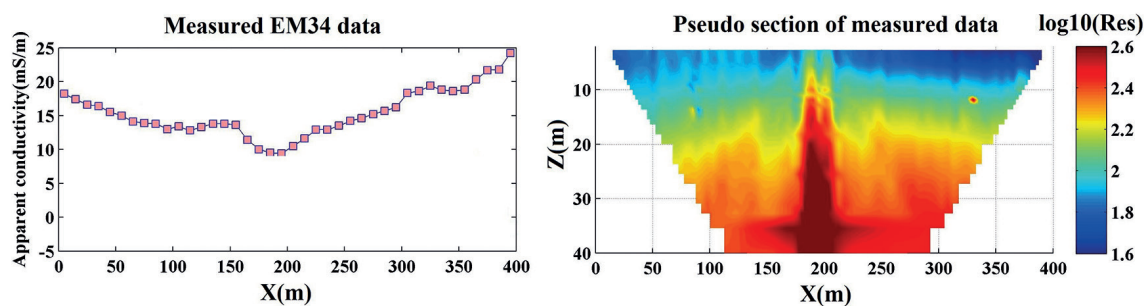
Fig. 14 - Measured data of both EM34 (on the left) and DC resistivity (on the right) approaches.
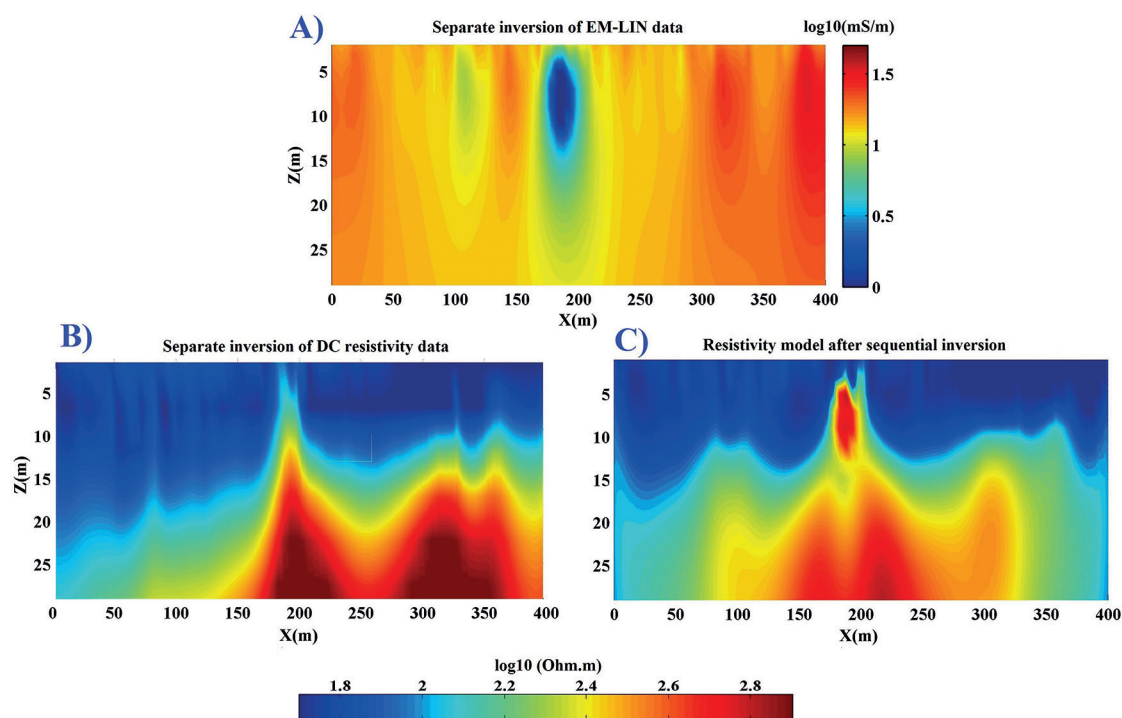

Fig. 15 - A) Individual (separate) inversion of EM-LIN data, B) separate inversion of DC resistivity datasets, and C) sequential inversion of DC resistivity model constrained by the EM-LIN method.

and a two-layered medium, where the first layer is conductive and the second layer is resistive. Ultimately, we should say that this real-world case was highly instructive for investigating different combinations of geophysical data. The RMS misfit errors of computed data compared to measured data for DC resistivity after separate and cooperative inversions are 5.12% and 6.23%, respectively, expressing that cooperative inversion (like cross-gradient joint inversion) acts as additional constraint to insert more bias in DC resistivity data inversion. Therefore, more RMS misfit errors are observed after cooperative inversion. The RMS misfit error of computed data for the EM-LIN method is 4.38%.

6. Discussion

The final section of this paper aims to justify the methodology employed in the study. Specifically, it explains why the tunnel case was chosen for joint interpretation, why sequential inversion of magnetometry and DC resistivity data was not performed, and why sequential inversion of DC resistivity and EM-LIN data was conducted. The text acknowledges that various combinations of datasets can be utilised, but it emphasises the strategic selection of methods for each case. For the first case, joint and sequential inversions of DC resistivity and gravity gradient datasets were attempted to enhance both the resistivity inverse model and the density model. However, the improved resistivity model did not offer any significant advantage over the density model obtained from a single inversion of gravity gradient data.

To further elucidate this point, Fig. 16 presents joint inverse models of DC resistivity and gravity gradient data. These models unequivocally demonstrate that none of the joint models are superior to the density model obtained from a single inversion of gravity gradient data, as shown in Fig. 7. Consequently, it is reasonable to conclude that for this particular case, sequential or joint inversion is not necessary.
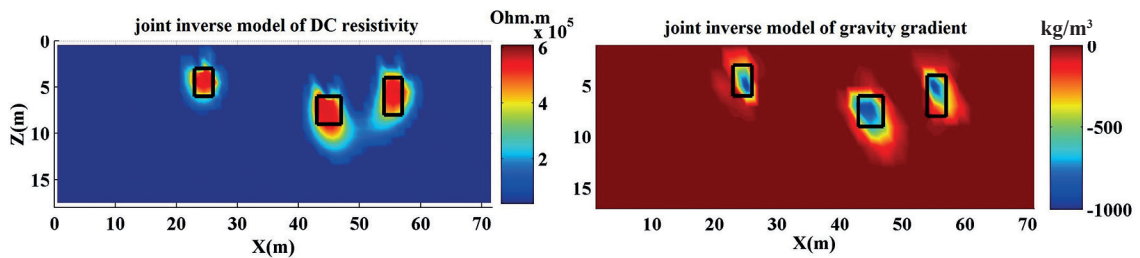

Fig. 16 - Joint inverse models for the tunnel case. None of these joint models are better than the individual inversion derived from the gravity gradient data shown in Fig. 9

Conversely, for the second and third cases:

I) Superiority of sequential and joint procedures

The resistivity models derived from sequential and joint inversion procedures are superior to all separate inversions available. Therefore, the applications of sequential and joint inversions are logical and reasonable in these cases.

II) Advantages of sequential EM-LIN and DC resistivity inversion

Since resistivity is the inverse of conductivity, the sequential inversion of EM-LIN and DC resistivity data is more convenient and reasonable than the sequential inversion of DC resistivity and magnetometry data. This is due to the fact that transforming the conductivity model (inversion of EM-LIN data) into a resistivity model, which is, then, used as the initial model for the sequential inversion process, is a straightforward procedure. In contrast, producing an initial resistivity model from an inverted susceptibility model requires some subjectivity and introduces more bias into the sequential inversion procedure. Therefore, the sequential inversion of EM-LIN and DC resistivity data is a more objective and reliable approach.

7. Conclusions

Accurate interpretation requires the combination of geophysical datasets since, in many cases, a single geophysical dataset does not provide sufficient information about underground sources. The combination of disparate geophysical datasets can be achieved through sequential inverse modelling, joint interpretation, and joint inversion. In this paper, all these types of data integration techniques were employed for two datasets, one from Iran and one from South Africa, to investigate their performance. The use of multiple data integration approaches enables a more comprehensive and reliable interpretation of the subsurface characteristics in these study areas.

The first real case includes measured apparent resistivities and gravity gradient data along a profile to reveal three tunnels at different depth ranges. The DC resistivity inverse model provides sufficient resolution to identify one of the tunnels, but the other two tunnels are not differentiated from each other. In contrast, the inverted density models show all three tunnels in their correct spatial positions. Through the joint interpretation of the two inverse sections, the high resistivity values and negative gravity anomalies can be used as indicators of the presence of the three tunnels (or cavities). This integrated approach, combining the information from both the resistivity and gravity gradient data, enables a more comprehensive and accurate identification of the subsurface features compared to using a single geophysical method alone.

The second real case includes DC resistivity, magnetometry, and EM-LIN datasets to recover a dolerite dyke immersed in the layered background. This dyke is an indicator of the presence of groundwater in the Morgenzon Farm site in South Africa. The datasets collected in the Morgenzon Farm enable:

I) joint inversion of DC resistivity and magnetometry. The authors performed a joint inversion of the DC resistivity and magnetometry datasets;

II) sequential inversion of DC resistivity and EM-LIN.

Additionally, a sequential inversion of the DC resistivity and EM-LIN data was conducted. This approach is more logical and straightforward than the sequential inversion of DC resistivity and magnetometry data as resistivity is the inverse of conductivity. Transforming the conductivity model (inversion of EM-LIN data) into a resistivity model, which is, then, used as the initial model for the sequential inversion process, is a more direct and less subjective procedure compared to producing an initial resistivity model from an inverted susceptibility model. The academic paraphrasing emphasises the complementary nature of the different geophysical datasets and the advantages of employing both joint inversion and sequential inversion techniques to characterise the subsurface features such as, in this case, the dolerite dyke which is indicative of the presence of groundwater in the Morgenzon Farm site.

The DC resistivity inversion shows a two-layered medium: a conductive top layer above a resistive layer. The inverse results of the magnetometry and EM-LIN datasets reveal a magnetised/resistive dolerite dyke with depth ranges from 3 to 15 m, while the dyke recovered by the EM-LIN data appears to be thicker. The resistivity models derived from both joint and sequential inversions show a dolerite dyke in a two-layered medium, where the dyke extends near to the surface. Overall, it can be said that these joint and sequential resistivity models are in satisfactory correspondence with each other.

REFERENCES

Al Farajat M.; 2009: *Characterization of a coastal aquifer basin using gravity and resistivity methods: a case study from Aqaba in Jordan*. Acta Geophys., *57*, 454-475.

Aster R.C., Borchers B. and Thurber C.H.; 2018: *Parameter estimation and inverse problems*. *3a ed.* Elsevier, Amsterdam, The Netherlands, 330 pp.

Bennington N.L., Zhang H., Thurber C.H. and Bedrosian P.A.; 2015: *Joint inversion of seismic and magnetotellurics data in the Parkfield region of California using the normalized cross-gradient constraint*. Pure Appl. Geophys., 172, 1033-1052.

Blakely R.J.; 1996: *Potential theory in gravity and magnetic applications*. Cambridge University Press, Cambridge, UK, 460 pp.

Boulanger O. and Chouteau M.; 2001: *Constraints in 3D gravity inversion.* Geophys. Prospec., 49, 265-280.

Cella F. and Fedi M.; 2012: *Inversion of potential field data using the structural index as weighting function rate decay*. Geophys. Prospect., 60, 313-336.

Ebrahimi A., Dehghan M.J. and Ashtari A.; 2019: *Contribution of gravity and Bristow methods for Karez (aqueduct) detection*. J Appl. Geophys., 161, 37-44.

Fregoso E. and Gallardo L.A.; 2009: *Cross gradients joint 3D inversion with applications to gravity and magnetic data*. Geophys., 74, 31-42.

Gallardo L.A.; 2004: *Joint two-dimensional inversion of geo-electromagnetic and seismic refraction data with cross-gradients constraint.* Doctoral dissertation, University of Lancaster, Lancaster, UK.

Gallardo L.A. and Meju M.A.; 2003: *Characterization of heterogeneous near-surface materials by joint 2D inversion of dc resistivity and seismic data*. Geophys. Res. Lett., 30, 1658.

Gallardo L.A. and Meju M.A.; 2004: *Joint two-dimensional DC resistivity and seismic travel time inversion with cross gradients constraints*. Journal of Geophysical Research Solid Earth., 109, B03311.

Gallardo L.A. and Meju M.A.; 2007: *Joint two-dimensional cross-gradient imaging of magnetotellurics and seismic traveltime data for structural and lithological classification*. Geophys. J. Int., 169, 1261-1272.

Gambetta M., Armadillo E., Carmisciano C., Stefanelli P., Cocchi L. and Tontini F.C.; 2011: *Determining geophysical properties of a near-surface cave through integrated microgravity vertical gradient and electrical resistivity tomography measurements*. J. of Cave and Karst Studies, 73, 11-15.

Ghari H., Varfinezhad R. and Parnow S.; 2023: *3D joint interpretation of potential field, geology, and well data to evaluate a salt dome in the Qarah-Aghaje area, Zanjan, NW Iran*. Near Surface Geophys., 21, 233-246.

Ghiasi S.M., Hosseini S.H., Afshar A. and Abedi M.; 2023: *A novel magnetic interpretational perspective on charmaleh iron deposit through improved edge detection techniques and 3D inversion approaches*. Nat. Resour. Res., 32, 147-170.

Ghose R. and Slob E.C.; 2006: *Quantitative integration of seismic and GPR reflections to derive unique estimates for water saturation and porosity in subsoil.* Geophysical Research Letters., 33, L05404, doi:10.1029/2025 GL025376.

Hosseini S.H., Habibian Dehkordi B., Abedi M. and Oskooi B.; 2021: *Implications for a geothermal reservoir at Abgarm, Mahallat, Iran: magnetic and magnetotelluric signatures*. Nat. Resour. Res., 30, 259-272.

Hu W., Abubakar A. and Habashy T.M.; 2009: *Joint electromagnetic and seismic inversion using structural constraints*. Geophys., 74, R99-R109.

Joulidehsar F., Moradzadeh A. and Doulati Ardejani F.; 2018: *An improved 3D joint inversion method of potential field data using cross-gradient constraint and LSQR method*. Pure Appl. Geophys., 175, 4389-4409.

Karavul C., Dedebali Z., Keskinsezer A. and Demirkol A.; 2010: *Magnetic and electrical resistivity image survey in a buried Adramytteion ancient city in western Anatolia, Turkey.* Int. J. Phys. Sci., 5, 876-883.

Last B.J. and Kubik K.; 1983: *Compact gravity inversion*. Geophys., 48, 713-721.

Le C.V.A., Harris B., Pethick A.M., Takougang E.M.T. and Howe B.; 2016: *Semiautomatic and automatic cooperative inversion of seismic and magnetotellurics data.* Surv. Geophys., 37, 845-896.

Li Y. and Oldenburg D.W.; 1996: *3-D inversion of magnetic data*. Geophys., 61, 394-408.

Makhokha D. and Fourie F.; 2016: *A systematic approach to the interpretation of conductivity anomalies across intrusive dolerite dykes and sills in the Karoo Supergroup.* MSc Thesis, in Geological Sciences, University of the Free State, Bloemfontein, South Africa.

McCarthy T. and Rubidge T.M., 2005: *The story of earth and life*. *1st ed.*, Struik Nature, Cape Town, 334 pp, doi:10.1017/500167568080047.06.

Milano M., Varfinezhad R., Bizhani H., Moghadasi M., Kalateh A.N. and Baghzendani H.; 2021: *Joint interpretation of magnetic and gravity data at the Golgohar mine in Iran*. J. Appl. Geophys., 195, 104476.

Molodtsov D.M., Troyan V.N., Roslov Y.V. and Zerilli A.; 2013: *Joint inversion of seismic traveltimes and magnetotellurics data with a directed structural constraint*. Geophys. Prospec., 61, 1218-1228.

Ogaya X., Alcalde J., Marzán I., Ledo J., Queralt P., Marcuello A., Martí D., Saura E., Carbonell R. and Benjumea B.; 2016: *Joint interpretation of magnetotellurics, seismic, and well-log data in Hontomín (Spain)*. Solid Earth, 7, 1-15.

Orfanos C. and Apostolopoulos G.; 2011: *2D-3D resistivity and microgravity measurements for the detection of an ancient tunnel in the Lavrion area, Greece*. Near Surf. Geophys., 9, 449-457.

Orlando L.; 2005: *Joint interpretation of geophysical data for archaeology: a case study.* Subsurf. Sens. Tech. Appl., 6, 235-250.

Paoletti V., Ialongo S., Florio G., Fedi M. and Cella F.; 2013: *Self-constrained inversion of potential fields.* Geophysical Journal International., 195(2), 854-869.

Parnow S., Oskooi B. and Florio G.; 2021: *Improved linear inversion of low induction number electromagnetic data.* Geophys. J. Int., 224, 1505-1522.

Perez-Flores M.A., Méndez-Delgado S. and Gomez-Treviño E.; 2001: *Imaging low frequency and dc electromagnetic fields using a simple linear approximation*. Geophys., 66, 1067-1081.

Singh A., Mishra P.K. and Sharma S.P.; 2019: *2D cooperative inversion of direct current resistivity and gravity data: a case study of uranium bearing target rock*. Geophys. Prospect., 67, 696-708.

Sultan S.A., Santos F.A.M. and Abbas A.M.; 2010: *Joint inversion interpretation for gravity and resistivity data: a case study at New Heliopolis City, Cairo, Egypt*. Near Surf. Geophys., 8, 43-53.

Tikhonov A.N. and Arsenin V.I.; 1977: *Solutions of ill-posed problems.* SIAM Review, 21, 266-267.

Varfinezhad R. and Ardestani V.E.; 2022: *Kernel based regularization parameter and source dependent depth weighting in gravity data inversion*. Bull. Geoph. Ocean., 63, 249-26

Varfinezhad R. and Oskooi B.; 2020: *2D DC resistivity forward modeling based on the integral equation method and a comparison with the RES2DMOD results*. J. Earth Space Phys., 45, 43.

Varfinezhad R. and Parnow S.; 2021: *3D Electromagnetic low induction number modeling using integral equations.* Journal of the Earth and Space Physics., 47(4), 99-110.

Varfinezhad R., Oskooi B. and Fedi M.; 2020: *Joint inversion of DC resistivity and magnetic data, constrained by cross gradients, compactness and depth weighting*. Pure Appl. Geophys., 177, 4325-4343.

Varfinezhad R., Fedi M. and Milano M.; 2022: *The role of model weighting functions in the gravity and DC resistivity inversion.* IEEE Transactions on Geoscience and Remote Sensing., 60, 1-15.

Varfinezhad R., Parnow S., Florio G., Fedi M. and Mohammadi Vizheh M.; 2023: *DC resistivity inversion constrained by magnetic method through sequential inversion.* Acta Geophys., 71, 247-260.

Vegter J.R.; 1992: *An evaluation of ground water exploitation and its potential for urban use. De Aar*. Hydrogeological Consulting Report to the Directorate of Geohydrology, Department of Water Affairs, Gezina, Pretoria, South Africa.

Woodford A. and Chevallier L. (eds); 2002: *Hydrogeology of the main Karoo basin: current knowledge and future research needs.* Water Research Commission, GEZINA, Report TT 179\02, 506 pp.

Zhang G., Lu Q.T. and Zhang G.B.; 2018: *Joint Interpretation of geological, magnetic, AMT, and ERT data for mineral exploration in the northeast of inner Mongolia, China*. Pure Appl. Geophys., 175, 989-1002.

Corresponding author: Ahmad Zarean Shirvanehdeh
                            Department of Civil Engineering
                            Shabestar Branch, Islamic Azad University
                            Shabestar, East Azerbaijan
                            Phone: +98 914 1197128; e-mail: Ah.zarean@iau.ac.ir